

Scale statistics of current sheets in relativistic collisionless plasma turbulence

Roberto F. Serrano¹ , Joonas Nättilä^{2,3,4}  and Vladimir Zhdankin^{5,4} 

¹Department of Natural Sciences, LaGuardia Community College, City University of New York, 31-10 Thomson Ave, Long Island City NY 11101, USA

²Department of Physics, University of Helsinki, P.O. Box 64, Helsinki FI 00014, Finland

³Physics Department and Columbia Astrophysics Laboratory, Columbia University, 538 West 120th Street, New York NY 10027, USA

⁴Center for Computational Astrophysics, Flatiron Institute, 162 Fifth Avenue, New York, NY 10010, USA

⁵Department of Physics, University of Wisconsin-Madison, Madison WI 53706, USA

Corresponding author: Roberto Serrano; rserrano125@gmail.com

(Received 19 August 2024; revision received 26 January 2025; accepted 27 January 2025)

We analyse distributions of the spatial scales of coherent intermittent structures – current sheets – obtained from fully kinetic, two-dimensional simulations of relativistic turbulence in a collisionless pair plasma using unsupervised machine-learning data dissection. We find that the distribution functions of sheet length ℓ (longest scale of the analysed structure in the direction perpendicular to the dominant guide field) and curvature r_c (radius of a circle fitted to the structures) can be well-approximated by power-law distributions, indicating self-similarity of the structures. The distribution for the sheet width w (shortest scale of the structure) peaks at the kinetic scales and decays exponentially at larger values. The data shows little or no correlation between w and ℓ , as expected from theoretical considerations. The typical r_c depends linearly on ℓ , which indicates that the sheets all have a similar curvature relative to their sizes. We find a weak correlation between r_c and w . Our results can be used to inform realistic magnetohydrodynamic subgrid models for plasma turbulence in high-energy astrophysics.

Keywords: Astrophysical Plasmas, Plasma nonlinear phenomena, Plasma simulation

1. Introduction

Over the last few decades, an increase in computational power has led to larger and larger direct numerical simulations of magnetohydrodynamic (MHD) turbulence (Biskamp 2008; Beresnyak 2019; Schekochihin 2022). While these simulations generally support the theory of Goldreich & Sridhar (1995) for self-similar fluctuations in MHD turbulence, the same simulations also show the presence of transient coherent structures – spatiotemporal fluctuations known as the intermittency (see, e.g., Vlahos & Isliker (2023), for a review). Among these coherent structures

are current sheets, which are ribbon-shaped regions of high electric current density. Current sheets have also been identified in simulations of collisionless plasmas where the full kinetic equations are solved (e.g., Comisso & Sironi 2018, 2019).

Several groups have performed statistical studies of current sheets in MHD turbulence to categorize their geometric distributions (Servidio *et al.* 2010; Uritsky *et al.* 2010; Zhdankin *et al.* 2013, 2014, 2016, 2017a; Ross & Latter 2018). They measured the distribution of the width, length and thickness of the current sheets. The results revealed that the current sheets are indeed self-similar structures, and their geometric components obey power-law or exponential distributions. In addition, recent works have detected and analysed current sheets in collisionless regimes (Makwana *et al.* 2015; Azizabadi, Jain & Büchner 2021; Sisti *et al.* 2021; Bussov & Nättälä, 2021). Others have also attempted to associate the properties of current sheets with the statistical distribution of turbulent field fluctuations, including recent works on relativistic MHD (Chernoglazov, Ripperda & Philippov 2021) and kinetic turbulence (Davis, Comisso & Giannios 2024).

Here, we focus on current sheets in fully kinetic simulations of magnetically dominated (relativistic) plasma turbulence. In the magnetically dominated regime, a large reservoir of magnetic energy is available to cascade down and dissipate, leading to heating and acceleration of non-thermal particles. None of the previous studies have performed the geometric statistical analysis in this regime of turbulence, which has $v_A \approx c$, where v_A is the Alfvén velocity and c is the speed of light. Relativistic kinetic turbulence is an area of active study in recent years, spurred by progress with particle-in-cell (PIC) simulations (Zhdankin *et al.* 2017b; Comisso & Sironi 2018; Nättälä & Beloborodov, 2021; Vega *et al.* 2022; Meringolo *et al.* 2023; Singh *et al.* 2024). It is relevant for many high-energy astrophysical systems (e.g., compact objects and transients). The motivation of this study is to perform a two-dimensional (2-D) statistical analysis of current sheets and compare/contrast with previous results in the literature.

In this article, we apply the computer vision algorithm developed by Bussov & Nättälä (2021) to 2-D fully kinetic (PIC) simulations of relativistic turbulence in pair plasmas. Notably, we measure the distributions of spatial scales of current sheets in the relativistic regime of kinetic turbulence. Section 2 describes the fundamental time scales and length scales and presents analytical expectations for the statistical scalings. In § 3, we discuss the numerical set-up of our PIC simulations, review the machine-learning segmentation algorithm and define our spatial scale measurements. In § 4, we present our measured distributions and their scaling indices. In § 5, we discuss the similarities between our scaling indices and previous studies and the implications for high-energy astrophysical plasmas.

2. Plasma length and time scales

We analyse the properties of current sheets in collisionless electron–positron pair plasmas. We consider pair plasma with an average temperature $\langle T \rangle$ (angular brackets $\langle \cdot \rangle$ indicate spatial averages in the remainder of the paper). Then, the average dimensionless temperature is given by

$$\theta \equiv \frac{k_B \langle T \rangle}{m_e c^2}, \quad (2.1)$$

where k_B is the Boltzmann constant, m_e is the electron mass and c is the speed of light.

The plasma is magnetized by threading it with a uniform background field $\mathbf{B}_0 = B_0 \hat{\mathbf{z}}$. The dimensionless parameter quantifying the strength of the magnetic field is the magnetization, given by

$$\sigma_0 \equiv \frac{B_0^2}{4\pi n_0 m_e c^2}, \quad (2.2)$$

where n_0 is the total particle number density.

The microscopic time scale of the plasma is characterized by the (cold) plasma frequency,

$$\omega_p \equiv \left(\frac{4\pi n_0 e^2}{m_e} \right)^{1/2}, \quad (2.3)$$

where e is the electron charge. In relativistic plasmas, the plasma frequency also defines the microscopic length scale of the system, known as the plasma skin depth,

$$\frac{c}{\omega_p} = \left(\frac{m_e c^2}{4\pi n_0 e^2} \right)^{1/2}. \quad (2.4)$$

The (non-relativistic) gyrofrequency is

$$\omega_B = \frac{eB_0}{m_e c}. \quad (2.5)$$

The related gyroradius is

$$r_g \equiv \frac{c}{\omega_B} \frac{\langle p \rangle}{m_e c} = \sigma_0^{-1/2} \frac{c}{\omega_p} \frac{\langle p \rangle}{m_e c}, \quad (2.6)$$

where p is the momentum of the particle. In the following, we use the skin depth c/ω_p as the reference scale when measuring sizes. This choice is made because c/ω_p is the largest of the kinetic scales when $\sigma_0 > 1$, thus determining the characteristic width of structures.¹

2.1. Current sheet distributions

The predominant intermittent structures in magnetically dominated plasma turbulence are current sheets.² In MHD turbulence, these structures are responsible for a large fraction of the overall resistive dissipation (e.g., Zhdankin, Boldyrev & Uzdensky 2016). In collisionless plasmas, they are likewise thought to be sites of energy dissipation through either magnetic reconnection or other kinetic damping mechanisms (e.g., Wan *et al.* 2012; TenBarge & Howes 2013; Howes 2016;

¹The formal relativistic versions of expressions (2.3) to (2.6) would have the average Lorentz factor of $\langle \gamma \rangle = \langle (1 - v^2/c^2)^{-1/2} \rangle$ in front of the masses, where v is the particle velocity in the system rest frame, and the brackets denote an average over particles.

²Apart from the electric current, $\mathbf{J} \propto \nabla \times \mathbf{B}$, vorticity of the velocity field, $\boldsymbol{\zeta} \equiv \nabla \times \mathbf{v}$, can be used to characterize the local ‘rotation’ of the flow. In an analogue to current sheets, intermittent vorticity sheets exist in plasma turbulence. We do not discuss vorticity sheets here since we focus on magnetically dominated plasmas.

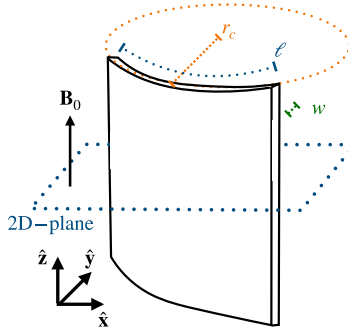


FIGURE 1. Schematic illustration of a 3-D current sheet along a background magnetic field \mathbf{B}_0 . The two directions perpendicular to the magnetic field are denoted with the 2-D plane. The length ℓ of a sheet (blue curved segment), followed by the width of the sheet w (green line), and the radius of curvature r_c (orange line).

Parashar & Matthaeus 2016; Loureiro & Boldyrev 2017; Mallet, Schekochihin & Chandran 2017; Ripperda *et al.* 2021; Nättilä & Beloborodov 2022; Borgogno *et al.* 2022; Chernoglazov, Hakobyan & Philippov 2023; Comisso & Jiang 2023; Davis *et al.* 2024).

In domains with the full three spatial dimensions, current sheets have a ribbon-like morphology and, therefore, can be ideally characterized by three scales (ignoring curvature and finer structure). For 2-D simulations with an out-of-plane background magnetic field \mathbf{B}_0 , the largest scale is in the direction of \mathbf{B}_0 , which we will ignore. The remaining two scales are in the directions perpendicular to the background magnetic field; we use the terminology length ℓ and width w to describe these two scales, ordered such that $\ell > w$. See figure 1 for a schematic view of our general definitions. We emphasize that this differs from the terminology used in three-dimensional (3-D) studies.

Numerical simulations of MHD turbulence exhibit current sheets that have a broad distribution of possible values of ℓ , spanning the turbulent inertial range; in particular, the data are well-described by a power-law distribution when ℓ is in the inertial range,

$$P_\ell(\ell) \equiv \frac{dN_{\text{sheets}}}{d\ell} \propto \ell^{-\alpha}, \quad (2.7)$$

where $N_{\text{sheets}} = \int P_\ell(\ell) d\ell$ is the number of sheets, and $\alpha \approx 3.3$ is measured in MHD turbulence simulations (Zhdankin *et al.* 2016). We note that α is used as a general index for any power-law distribution in the following text. The widths, on the other hand, mainly reside near the dissipation scale s , with a narrowly peaked distribution, which we will approximate as

$$P_w(w) \equiv \frac{dN_{\text{sheets}}(w)}{dw} \propto \exp\left(-\frac{w}{s}\right), \quad (2.8)$$

where $s \sim c/\omega_p$. Furthermore, we measure the circular curvature of the current sheets, r_c , which may be expected to be a power-law distribution,

$$P_{r_c}(r_c) \equiv \frac{dN_{\text{sheets}}}{dr_c} \propto r_c^{-\alpha}, \quad (2.9)$$

because the structures are distorted by turbulent eddies spanning a broad range of scales. The power-law index for $P_{r_c}(r_c)$ is non-trivial to predict from theory. In addition, we will be analysing the joint 2-D distributions,

$$P_{w,\ell}(w, \ell) \equiv \frac{\partial^2 N_{sheets}(w, \ell)}{\partial w \partial \ell}, \quad (2.10)$$

$$P_{w,r_c}(w, r_c) \equiv \frac{\partial^2 N_{sheets}(w, r_c)}{\partial w \partial r_c} \quad (2.11)$$

and

$$P_{r_c,\ell}(r_c, \ell) \equiv \frac{\partial^2 N_{sheets}(r_c, \ell)}{\partial r_c \partial \ell}, \quad (2.12)$$

which capture the correlations between ℓ , w and r_c . The one-dimensional (1-D) distributions follow naturally from the marginalization of these distributions as, for example, $P_w(w) = \int P_{w,\ell}(w, \ell) d\ell$. We anticipate that since $w \sim s \sim c/\omega_p$, the width will be weakly correlated (if at all) with the other scales. The correlation between r_c and ℓ is non-trivial to predict, in general, since structures of varying lengths will be distorted by different populations of turbulent eddies. However, we note that $r_c \propto \ell$ if the relative curvature of the structure is scale independent (i.e., the typical shape of a curved structure is independent of its length).

3. Methods

3.1. Numerical methods and set-up

We analyse the 2-D freely evolving (decaying) turbulence simulations presented in Nättilä & Beloborodov (2021). Here, we briefly review the simulation set-up, and initial conditions and refer the reader to the original paper for more details.

The simulations are initialized with a homogeneous pair plasma with a uniform density $n_{\pm,0}$ and an initial temperature $\theta_0 = 0.3$. The plasma is threaded by a uniform out-of-plane magnetic field $\mathbf{B}_0 = B_0 \hat{\mathbf{z}}$. To seed the turbulence, we perturb the magnetic field in the directions perpendicular to the magnetic field, $\mathbf{B}_\perp = (B_x, B_y, 0)$ with sinusoidal large-scale modes with wavelength $l_0 = L/8$ (where L is the size of the full simulation domain). The initial perturbation has amplitude $\mathbf{B}_\perp^{rms}/B_0 = 1$, where $\mathbf{B}_\perp^{rms} = \sqrt{\langle \mathbf{B}_\perp^2 \rangle}$.

The simulations use the relativistic PIC module in the Runko framework (Nättilä 2022). The PIC algorithm evolves all three components of the electromagnetic fields using a second-order finite-difference scheme, while particles evolve in time using a relativistic Boris pusher. These simulations are 2.5D; i.e., all three components of the particle momenta and fields are retained, while there is variation in only two spatial coordinates. In addition, we impose doubly periodic boundary conditions on the domain and perform eight passes of digital current filtering at each time step. The current filtering is performed immediately after the particle's current deposition using a three-point binomial filter to smooth out the numerical noise that results from a finite number of computational particles.

The 2-D domain in our simulations is a square in the x-y plane of size $L = 1024c/\omega_p$, and it is covered with 5120^2 cell resolution. The (initial) plasma skin depth is resolved by five grid cells. In our 2-D simulations, we initialize fluctuations on a

scale of $l_0 \approx 125c/\omega_p$. We simulate the turbulence for $20l_0/c$. We focus on two simulations with $\sigma_0 = 1$ and 10, which correspond to the transrelativistic (magnetically dominated) regime. During the simulation, the plasma heats up and so θ_0 increases (see figure 6 in Nättilä & Beloborodov (2021)). For our simulation with $\sigma_0 = 1$ at $t = l_0/c$, we measure $\theta \approx 0.45$ which then increases to $\theta \approx 0.60$ at $t = 15l_0/c$. Similarly, for the case of $\sigma_0 = 10$, we first measure $\theta \approx 0.50$ which then increases to $\theta \approx 2.70$. Thus, the temperatures become only mildly relativistic, and it is reasonable to use the non-relativistic expressions for kinetic scales from § 2.

We present six visualizations of one of our simulations with $\sigma_0 = 10$ at $t = 4.6 l_0/c$ in figure 2. The magnetic eddies are visible for the fully developed turbulence as large plasma over-densities (figure 2a). Secondly, we can visually trace out two types of structure in the out-of-the-plane current density component J_z (figure 2b): elongated stripes (current sheets) and circular spots (plasmoids). These same structures are also visible as coherent structures in the (perpendicular) magnetic field \mathbf{B}_\perp (figure 2c): the current sheets coincide with regions of alternating magnetic fields (in between colliding plasmoids). The plasmoids coincide with the location of magnetic loops. The regions with current sheets (with antiparallel fields) are prominent locations of energy dissipation. The sheet regions can be associated with areas of energy dissipation when visualizing the work done by the electric field $\propto \mathbf{J} \cdot \mathbf{E}$ (figure 2d). We note that a significant fraction of the regions with high electric currents have magnetic fields that are parallel (rather than antiparallel) on both sides (Ha *et al.* 2024).

A standard method to segment the current sheets into individual structures is to apply a threshold in the current density. To illustrate this method, we trace out the outlines of the sheets by applying a threshold of $J_z/J_{rms} > 3$ (figure 2e). In our case, however, we use the regions originating from a more advanced region-of-interest (ROI) detection (measured at a time $4l_0/c$), relying on a computer vision segmentation algorithm presented in Bussov & Nättilä (2021) (figure 2f). Such segmentation method has the advantage that it clusters the sheets based on not only the electric current but also other features; this enables us to separate the current sheets and plasmoid cores from each other. The details of the method are given in the next section.

3.2. Overview of the machine-learning algorithm

We employ the unsupervised ensemble machine-learning algorithm developed by Bussov & Nättilä (2021) to segment the current sheets from fully kinetic plasma turbulence simulations. The algorithm is an ensemble extension of the self-organizing map (SOM) algorithm (Kohonen 2001, 2013) dubbed ‘statistically combined ensemble’ (SCE), which merges multiple (independent) SOM evaluations together, hence increasing the robustness of the ROI boundaries.

Briefly, we outline how the algorithm works. We apply the SOM algorithm to our simulation snapshots and cluster the data using three features: \mathbf{B}_\perp , \mathbf{J}_z and $\mathbf{J}_z \cdot \mathbf{E}$, where \mathbf{B}_\perp is the (in-plane) perpendicular magnetic field, \mathbf{J}_z , is the (out-of-the-plane) parallel component of the current and $\mathbf{J}_z \cdot \mathbf{E}$ is a measure of the work done by the electric field \mathbf{E} . Each pixel on the image then defines a multidimensional feature-space data point.

The SOM algorithm is based on a 2-D network of neurons that are trained to approximate the multidimensional (feature-space) data. In practice, the map can be thought of as a (finite) surface that is fitted to the input data points. Conversely,

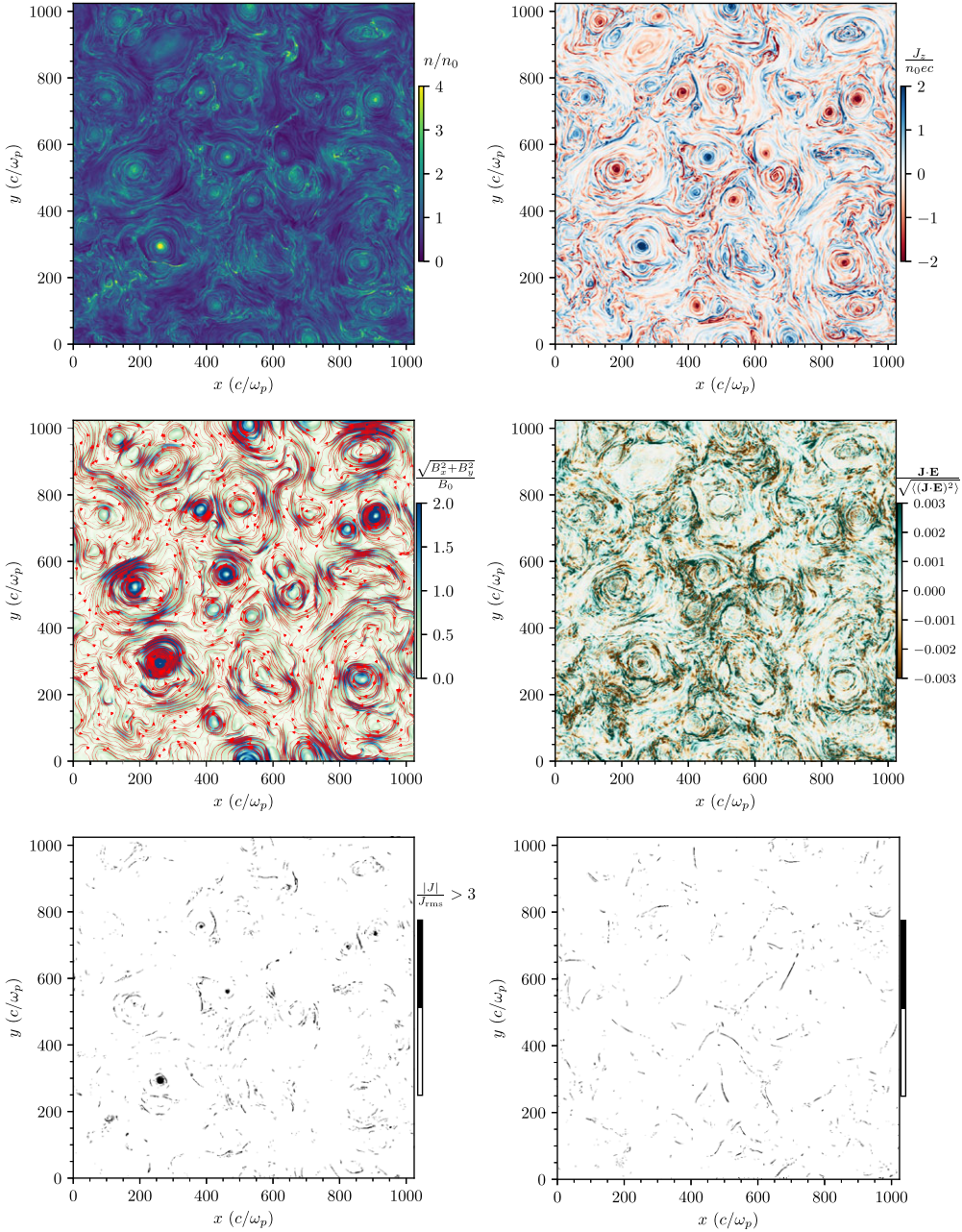


FIGURE 2. Visualization of the analysed turbulence data measured at time $t = 4.6l_0/c$: plasma density n/n_0 , where n_0 is the initial plasma density (a); out-of-the-plane current density J_z/n_0ec (b); strength of the in-plane magnetic field component $\sqrt{B_x^2 + B_y^2}/B_0$, and the field lines (red curves), where B_0 is the initial guide field strength (c); a proxy of the work done by the parallel electric field $\mathbf{J} \cdot \mathbf{E} / \sqrt{\langle (\mathbf{J} \cdot \mathbf{E})^2 \rangle}$ in units of the root mean square value (d); regions of the current density with $J/J_{rms} > 3$, where $J_{rms} = \sqrt{\langle J^2 \rangle}$ (e); and, current sheet regions from the SCE algorithm (f). The SCE algorithm is shown at $t = 4.0l_0/c$.

each feature-space data point can be associated with a best-matching neuron on the map. The map defines a latent (reduced) data space for the input data.

The neural map is then used to cluster the feature-space data into different groups by associating a region on the map (i.e., a set of connected neurons) as one data cluster. The (feature-space) distance between the neurons defines a convenient cost function to separate the neurons into a finite number of clusters. In theory, the number of resulting clusters is arbitrary. Still, in practice, the map often has distinct regions of closely connected neurons that help set the number of resulting clusters from the analysis. In our case, the SOM algorithm results, on average, in four distinct clusters, one of which is the current sheets (see, Bussov & Nättilä (2021) for more details).³

In practice, we use an ensemble version of the SOM to segment the sheets. This so-called SCE method combines multiple SOM segmentations into one clustering realization to increase the signal-to-noise ratio of each ROI boundary. In general, our machine-learning-based segmentation method should be contrasted with the previously used threshold technique, where the boundaries of the current sheets are found by setting a threshold value for the magnitude of the electric current (see figure 2*f*). We emphasize that our definition of a current sheet is more complex than what results, e.g., from segmenting the sheets with the threshold method: our definition of the current sheets is based on a combination of all three input features. The second reason, in addition to the more generic definition of the current sheet cluster, is that the SCE method is computationally faster, making it feasible to construct large structure catalogues. We note, however, that the algorithm is currently calibrated only on 2-D data, so we focus on that here.

3.3. Measurements

The following section presents our definitions of geometric length and width. Specifically, we analyse a time series of 2-D masks separated by $\Delta t = 1l_0/c$ for two simulations with $\sigma_0 = 1$ and $\sigma_0 = 10$. We analyse a time interval, $l_0/c \leq t \leq 15l_0/c$ when the turbulence is fully developed but still sustains large amplitude fluctuations. In practice, when analysing the structures, we use the open-source geometry library ‘Shapely’ (Gillies *et al.* 2024) to automate the geometric analysis of the structures. First, we dissect each independent closed contour in a mask into (x, y) coordinate lists that trace the element’s boundary. This procedure is repeated for every mask in the time series. Specifically, we use the Shapely.Polygon class, which takes a set of N_p data points and connects the chain of coordinate points into a ‘ring’. We generate an instance of this polygon class for each structure in a given image. Once we generate the Polygon class to represent the current sheet, we measure its perimeter $\mathcal{S} (= \oint ds$, where the line integral is performed along the closed curve around the polygon) and use it to define a robust estimator of the sheet length ℓ as

$$\mathcal{S} \approx 2\ell + 2w \approx 2\ell, \quad (3.1)$$

so that $\ell \approx \mathcal{S}/2$, where we assumed that $w \ll \ell$ in the second part of the equation. We also tried measuring ℓ by taking the pairwise distance between each coordinate point and identifying the largest distance as ℓ . However, we forgo this definition

³The clustering analysis also identifies plasmoids as a separate cluster. Here, we omit the analysis of that cluster because the chosen 2-D geometry makes the plasmoids longer-lived compared with three dimensions.

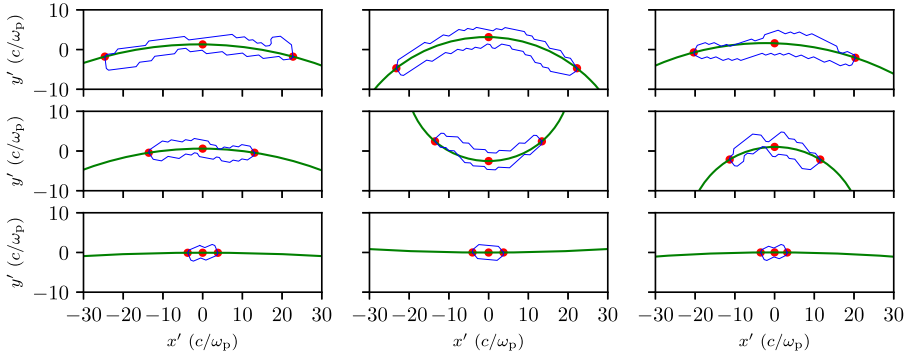


FIGURE 3. Examples of current sheets in our catalogue. Individual current sheets of varying length, ℓ , and radius of curvature, r_c , are visualized in the transformed position space (x', y') using (A1) and (A2). The three red points mark the locations used to calculate the curvature radius using (C2). The green line shows the arc of the circle passing through the three points, with the centre calculated using (C6).

since we find it to be a noisier estimator of ℓ . We also note that when accounting for the possible curvature of the structure, the natural length is the arclength of the structure, not the distance along the structure's longest dimension; therefore, our definition ℓ also naturally includes the curvature effects.

To measure the width (see [appendix A](#) for the full derivation), we take each structure and calculate the major axis of each sheet, which is defined as the largest distance between any set of points. Then, we rotate the structure such that its major axis lies on the x axis. Then, we translate the structure to the origin. Once in this new reference frame, we measure the width using (B1).

Finally, we introduce a measurement of the curvature of the current sheet, dubbed 'curvature radius', r_c . The radius of curvature is calculated by fitting a circle through the three points on the curve: leftmost point, centre point and rightmost point (in the new reference frame described above). Then, a circle with a radius r_c can be defined to pass through each point. In the limit that the curvature radius $r_c \rightarrow 0$, the structure is highly curved, and as $r_c \rightarrow \infty$, the structure becomes flat. We detail our simple circle fitting algorithm in [appendix C](#).

In [figure 3](#), we display representative examples from the resulting current sheet catalogue for the simulation with $\sigma_0 = 10$. These examples show that most of the sheets have approximately constant width w .

Lastly, the approximation of the sheet curvature as part of a circle's arc seems appropriate in almost all cases; in total, we find that only approximately 0.5 % of the sheets can not be adequately modelled as arcs (but are, e.g., S - or L -shaped). Such non-standard morphologies can sometimes result from the interactions and mergers of sheets.

4. Results

Our catalogue contains $\approx 13\,000$ individual objects for $\sigma_0 = 1$ and $\approx 10\,000$ for $\sigma_0 = 10$ simulations. Each time snapshot contains, on average, $\approx 1\,000$ current sheets and provide detailed time-dependent statistics of the structures. The total volume-integrated magnitude of the electric current closely traces the evolution of the decaying turbulence: for $t = 0$ to $\sim 3\,l_0/c$, we observe an initial transient

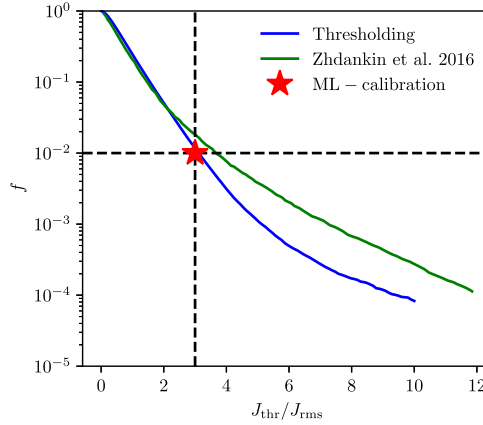


FIGURE 4. The filling fraction of current sheets, f , of our simulation of $\sigma_0 = 10$ measured at $4.6l_0/c$, as function of J_{thr}/J_{rms} (blue line), where J_{thr} is the threshold factor, and where $J_{rms} = \sqrt{\langle J^2 \rangle}$ is the root mean square of the current density. The star symbol denotes the filling fraction measured using our machine-learning algorithm. We also fit the MHD data from Zhdankin *et al.* (2016) (green line).

period where the turbulent structures form and the magnitude of the electric current rapidly grows; for $t \gtrsim 3 l_0/c$, the turbulence decays and the magnitude of the current decreases slowly (see also, e.g., Nätilä & Beloborodov 2021). The analysed current sheets are long-lived intermittent structures and their time evolution is analysed and discussed in more detail, e.g., in Imbrogno *et al.* 2024.

We calibrate our current sheet identification method with the previous method of ‘thresholding’ used in Zhdankin *et al.* (2014) and Zhdankin *et al.* (2016). In figure 4, we plot the volume filling fraction f of the structures occupying pixels having current densities $|\mathbf{J}| > J_{rms}$, where J_{rms} is a threshold parameter that we vary. The filling fraction of the structures with current densities above the threshold exhibits a steep exponential decay at low $J_{thr}/J_{rms} < 3$, which then flattens to a less steep decay for $J_{thr}/J_{rms} > 3$. We also compare our results with the MHD analysis by Zhdankin *et al.* (2016) which shows a very similar behaviour for $J_{thr}/J_{rms} > 3$. We find that the filling fraction of structures detected by the SCE algorithm agrees with the thresholding method when $J_{thr}/J_{rms} \approx 3$ (the red star in figure 4). This indicates the ‘effective’ threshold of the SCE algorithm.

In figure 5, we plot the width distribution, $P_w(w)$, of our current sheets for both values of $\sigma_0 = 1$ and 10. The distribution resembles an exponential distribution, peaking at around $3 c/\omega_p$. Qualitatively, the distributions are best modelled with an exponential function, $\exp(-w\omega_p/c)$. The width distribution does not greatly vary over time.

In figure 6, we visualize the length distribution of our current sheets, $P_\ell(\ell)$, and similarly to the width distribution, we find that the distribution remains roughly constant over time. The distribution can be modelled as a power-law distribution with an index, $\alpha = 2.5$. The distribution peaks at $5c/\omega_p$, and extends to $\sim 100 c/\omega_p$; i.e., close to the initial energy-carrying scale l_0 of the simulation.

Next, in figure 7, we visualize the curvature distribution $P_{r_c}(r_c)$ (although we omit structures with $\ell < 7.5c/\omega_p$ because the curvature measurement becomes unreliable for very short structures). The distribution is a clear power-law with an index

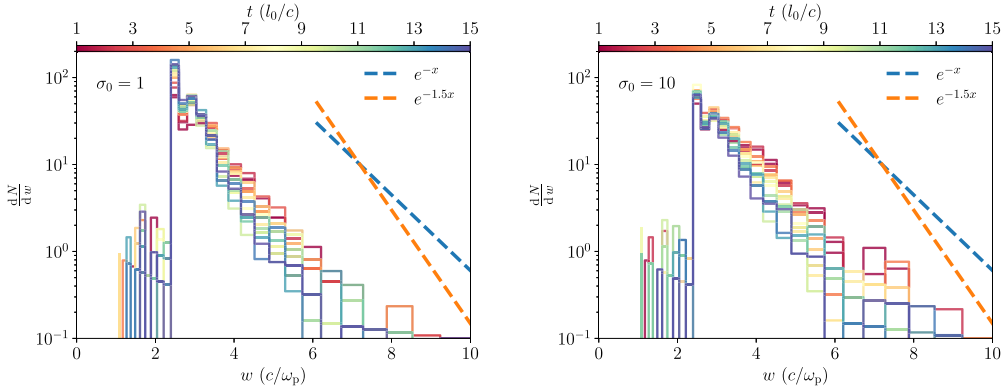


FIGURE 5. Width distributions, dN/dw , for simulations with initial $\sigma_0 = (1, 10)$. Two reference exponential fits with the corresponding index are shown in the legend.

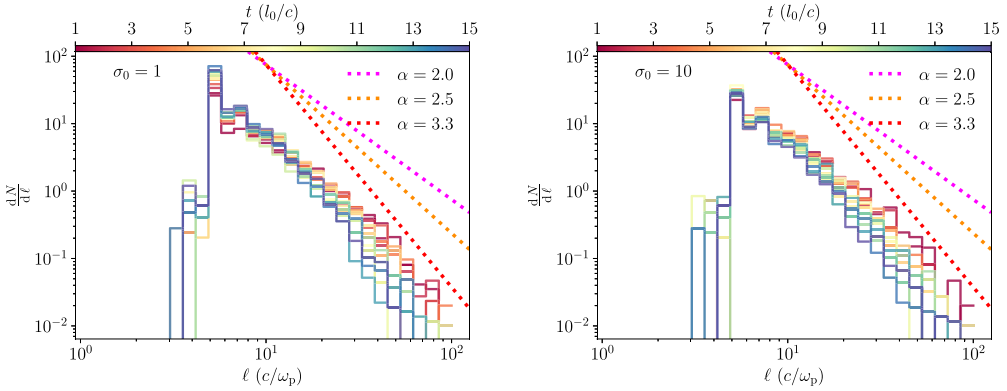


FIGURE 6. Length distribution, dN/dl , for simulations with initial $\sigma_0 = (1, 10)$. Three reference power laws with the corresponding index are shown in the legend.

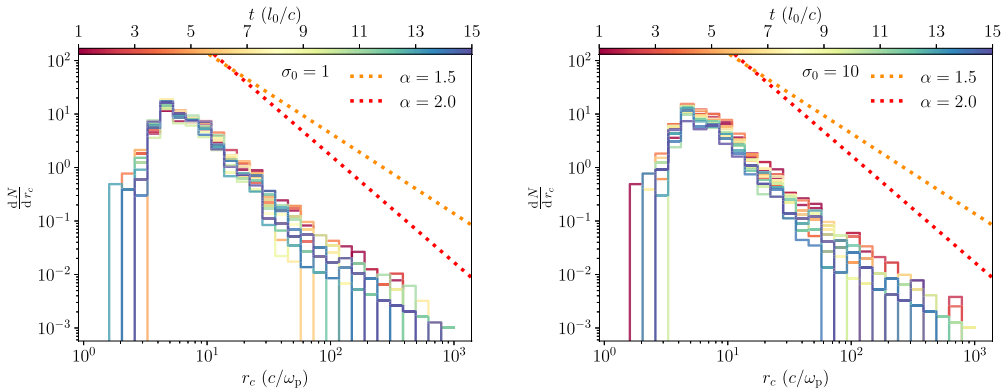


FIGURE 7. Radius of curvature distributions, dN/dr_c , for simulations with initial $\sigma_0 = (1, 10)$. Two reference power laws with the corresponding index are shown in the legend. This distribution is restricted to current sheets with $l > 7.5c/\omega_p$, to avoid spurious measurements from small structures.

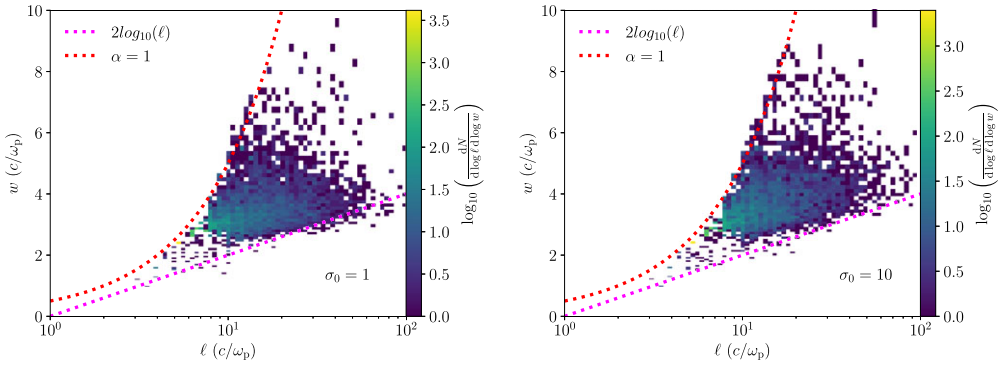


FIGURE 8. The 2-D histogram correlating the average width and length distributions for simulations with initial $\sigma_0 = 1, 10$. The power law index fits the distributions shown in the legend.

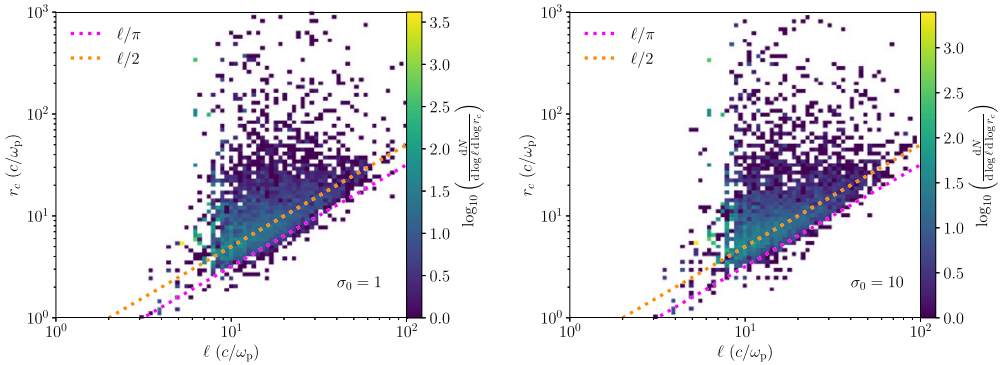


FIGURE 9. The 2-D histogram correlating the radius of curvature and length distributions for simulations with initial $\sigma_0 = 1, 10$. The power law index fits the distributions shown in the legend.

$\alpha = 2.0$. The distribution peaks at $3c/\omega_p$, and extends to approximately $1000c/\omega_p$. The distribution is steady in time, with no significant evolution.

Furthermore, we study the 2-D joint distributions of the width and length, $P_{w,\ell}(w, \ell)$, in figure 8. We find no clear scaling between the two quantities. The distribution is bounded such that the upper limits of the distribution are fit by $w \propto \ell^\alpha$, where $\alpha = 1.0$. We fit $2 \log_{10}(\ell)$ for the lower bound.

Similarly, in figure 9, we visualize the 2-D distributions of the curvature and length, $P_{r_c,\ell}(r_c, \ell)$. The mean value of the sheets linearly scales with ℓ (dark orange line). This suggests that the relative curvature to size is the same for all ℓ . Additionally, we find that the distribution can be traced with $r_c \propto \ell/\pi$. We also show a fit that corresponds to $r_c \propto \ell^\alpha/2$, where $\alpha = 1$. One final note is that at $\ell < 7c/\omega_p$ the curvature measurement becomes unreliable and one can see a small ‘cluster’ of points at $r_c \approx 100c/\omega_p$ and $r_c \approx 300c/\omega_p - 400c/\omega_p$.

Finally, in figure 10, we visualize the 2-D distribution of the width and curvature, $P_{w,r_c}(w, r_c)$. Here, no strong correlation is seen. The upper end of the distribution is traced with $w \propto \ell^\alpha$, where $\alpha = 1$. Since the structures have widths close to the

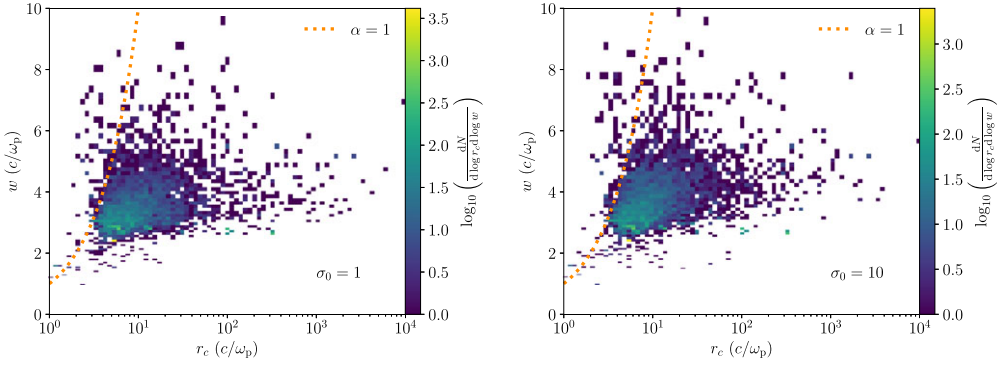


FIGURE 10. The 2-D histogram correlating the width and radius of curvature distributions for simulations with initial $\sigma_0 = 1, 10$. The power law index fits the distributions shown in the legend.

dissipation scale, it seems reasonable that they are independent of the curvature, which is more likely sensitive to MHD-scale fluctuations.

5. Discussion

We have analysed various length statistics of tens of thousands of current sheets found in freely evolving (decaying) plasma turbulence. In particular, we have found the following.

- (i) The current sheet length distribution has a power law tail with index $\alpha = 3.3$; it is shallower ($\alpha \approx 2$) at small lengths ($\ell \lesssim 30 c/\omega_p$).
- (ii) The width distribution is sharply peaked at $w \sim 3 c/\omega_p$; it resembles an exponential decay at higher w . There is a slight logarithmic increase of w as a function of ℓ .
- (iii) The characteristic curvature radius is $r_c \sim \ell/2$, hence the sheets are slightly curved. However, we find that short ($\ell \sim 10 c/\omega_p$) sheets are often flatter (larger r_c); hence, the curvature distribution is a shallower distribution than the length distribution (as seen by the 1-D histogram indices), with $\alpha = 2.0$.
- (iv) All distributions have weak (or no) time dependence as the turbulence evolves during the studied period of fully developed turbulence.
- (v) All distributions have weak (or no) magnetization dependency in the considered range $1 \leq \sigma_0 \leq 10$.
- (vi) In addition, we calibrated the machine-learning-based identification algorithm of Bussov & Näätä (2021) against the thresholding method. We found that the filling fraction of current sheets in our algorithm matches the thresholding method at a value of $J_{thr}/J_{rms} = 3$.

The limitations of our study are mainly due to our algorithm being 2-D. This is a simplification since, in this case, the sheets have a simpler topology to characterize. In three dimensions, the current sheets can have much more complex shapes. Ultimately, however, the analysis must be generalized to full three dimensions to obtain physically realistic sheet distributions.

Many possible extensions of the work can also be devised. For example, it is possible to measure plasma parameters (e.g., plasma- β , real magnetization σ , temperature T , the ratio of reversing field to guide field $\delta B/B_0$, etc.) upstream from the current sheet using the SCE algorithm, as done in Nurisso *et al.* (2023), to gather information about the particle acceleration conditions. The sheet statistics should also be studied in different parameter regimes by varying, e.g., the initial amplitude $\delta B/B$, helicity and plasma composition (e.g., using an electron–ion rather than pair plasma composition). In addition, different driving methods should be explored, such as via wave collisions or purely compressive/solenoidal driving. These are expected to change the turbulence intermittency and affect the sheet statistics. The presented work is, therefore, only the first step in this direction. The differences between the non-relativistic ($\sigma_0 \ll 1$) and ultrarelativistic ($\sigma_0 \gg 1$) regimes are not obvious and will require more parameter studies.

Our findings are relevant to a broad range of astrophysical systems because kinetic/MHD turbulence is also ubiquitous in those systems. Some problems where intermittency of kinetic/MHD turbulence plays a crucial role are as follows.

- (i) Black hole accretion flows and jets in low luminosity active galactic nuclei. Their environments are expected to be magnetized and turbulent (e.g., Näätäli 2024). Most of the current efforts in supermassive black-hole accretion flow modelling employ general relativistic MHD simulations (Event Horizon Telescope Collaboration *et al.* 2019). However, ideal fluid simulations cannot self-consistently model the temperature of electrons so the electron temperature profile is often ‘painted on’ via postprocessing (e.g., Mościbrodzka *et al.* (2016); however, see Galishnikova *et al.* (2023) for a recent fully kinetic general relativistic PIC simulations with realistic electron plasma physics). Alternatively, some general relativistic MHD simulations employ a variety of subgrid models to compute the electron and ion temperatures based on local PIC simulations of magnetic reconnection (Ball, Sironi & Özel 2018; Werner *et al.* 2018) or kinetic/MHD turbulent heating based models (Howes 2010; Kawazura, Barnes & Schekochihin 2019; Meringolo *et al.* 2023).
- (ii) The Crab pulsar wind nebula (PWN) is another example of a highly magnetized ($\sigma_0 \gtrsim 1$) environment that can accelerate particles to very high energies (Rees & Gunn 1974; Kennel & Coroniti 1984*a, b*; Atoyan 1999). Recently, in an attempt to resolve observational discrepancies of the Crab PWN with theoretical models, Luo *et al.* (2020) proposed a turbulent origin of the non-thermal emission in the Crab PWN.
- (iii) Cosmic ray diffusion in galactic environments, such as interstellar and inter-cluster mediums, strongly depends on the turbulence physics (Ruszkowski & Pfrommer 2023). It is still not understood what exactly scatters the cosmic rays. However, one hypothesis is the intermittent structures in the turbulence (Kempski *et al.* 2023; Lemoine 2023).

In summary, we have obtained the scaling distributions for the geometric properties of current sheets, including the length, width and radius of curvature. We find that the length and radius of curvature distributions are well-approximated as power-law distributions and the width distribution with an exponential function. This information can be used to develop realistic subgrid models for turbulent heating in the accretion flows of compact objects and other turbulent environments.

Acknowledgments

The authors thank the anonymous reviewers for their comments, which improved the quality of the manuscript. The authors also thank L. Sironi and T. Ha for their helpful discussions. R.S. is also thankful to Stack Overflow user (Scott), and the Flatiron Institute for Guest Researcher appointment.

Funding

This work is supported by an ERC grant (ILLUMINATOR, 101114623). V.Z. acknowledges support from NSF grant PHY-2409316. J.N. and V.Z. acknowledge support from a Flatiron Research Fellowship at the Flatiron Institute. Research at the Flatiron Institute is supported by the Simons Foundation.

Declaration of interests

The authors report that they do not have a conflict of interest.

Appendix A. Transformation to local coordinate frame

In this appendix, we describe the local coordinate system constructed for presenting example current sheets in [figure 3](#) and for measuring the width. This coordinate system is defined individually for each structure.

For each current sheet, we first need the perimeter points of the polygon, (x_i, y_i) with $i \in \{1, \dots, N_p\}$, where N_p is the number of perimeter points identified by the SOM algorithm.⁴ First, we identify the left-hand (or right-hand) edges of the polygon by finding the index i_L (or i_R) at which x_i takes a minimal (or maximal) value in the set $\{x_i\}$; we denote the (Euclidean) distance between these points by $r_x = [(x_{i_R} - x_{i_L})^2 + (y_{i_R} - y_{i_L})^2]^{1/2}$. Likewise, we identify the bottom (or top) edge of the polygon by finding the index i_B (or i_T) at which y_i takes a minimal (or maximal) value in the set $\{y_i\}$; we denote the distance between these points by $r_y = [(x_{i_T} - x_{i_B})^2 + (y_{i_T} - y_{i_B})^2]^{1/2}$. The ‘major axis’ is then defined by the larger of r_x and r_y .⁵

Next, we transform to a new coordinate system (x', y') such that the centre of the polygon and the major axis is along the x' -axis. To achieve this, we define a vector \mathbf{D} that is oriented along the major axis,

$$\mathbf{D} = \begin{cases} \frac{(x_{i_R} - x_{i_L}, y_{i_R} - y_{i_L})}{r_x} & r_x > r_y \\ \frac{(x_{i_T} - x_{i_B}, y_{i_T} - y_{i_B})}{r_y} & \text{otherwise} \end{cases} \quad (\text{A1})$$

and a rotation matrix

$$M = \begin{bmatrix} D_x & D_y \\ -D_y & D_x \end{bmatrix}. \quad (\text{A2})$$

⁴Here, two special cases need to be discussed: (i) What happens if multiple points satisfy the criterion for being the maximum or minimum coordinates? This tends to be the case for structures with complex topologies (e.g. if the structure is a branchlike shape or deformed). We checked that these include at most ≈ 60 sheets out of our sample. Thus, they are statistically negligible, and we will ignore them. (ii) How to account for the splitting of structures when they cross the periodic boundary of the simulation? For simplicity, we do not account for this; However, in that case, it should be noted that these structures are double-counted. We verified that there are $O(10)$ such sheets per time step, so they are not expected to influence our analysis.

⁵Note that this procedure is not coordinate invariant since it treats separations along the x and y directions as special.

To transform to the new coordinates (x', y') for each structure, we multiply the original coordinates (x, y) by the rotation matrix M and then subtract the structure's 'average' location from its position coordinates,

$$(x'_i, y'_i) = M \cdot (x_i, y_i) - (\langle x_i \rangle, \langle y_i \rangle), \quad (\text{A3})$$

where $\langle x_i \rangle$ and $\langle y_i \rangle$ are the mean location values from the sets x_i , and y_i , respectively.

Appendix B. Algorithm for measuring the sheet width

Continuing the calculation from [appendix A](#), we are now in the local coordinate frame (x'_i, y'_i) . In this frame, we calculate the width of each current sheet. First, we must reidentify the left-hand (or right-hand) edges of the polygon in the local coordinate frame; i'_L (or i'_R) at which x'_i takes a minimal (or maximal) value in the set $\{x'_i\}$ of points on the structure's perimeter. Likewise, we reidentify the bottom (or top) edge of the polygon by finding the index i'_B (or i'_T) at which y'_i takes a minimal (or maximal) value in the set $\{y'_i\}$.

One simple method to calculate the width would be to take the (Euclidean) distance between the points $(x'_{i'_T}, y'_{i'_T})$ and $(x'_{i'_B}, y'_{i'_B})$. However, this definition may not represent the overall structure if the current sheet's width varies along its length.

Therefore, to define a better representation of the overall width, we take the additional step of breaking each current sheet into vertical strips and averaging the width across the strips. The first step is to divide each sheet into a 'top' half and 'bottom' half along the direction parallel to x'_i . We begin from $x'_{i'_L}$, and find its y' -coordinate $y'_{i'_L}$, and similarly, we take $x'_{i'_R}$ and find its y' -coordinate pair $y'_{i'_R}$. Next, we begin sorting the y' -coordinate pairs into two new arrays, $y_{i,\text{top}}$ and $y_{i,\text{bot}}$ in the following manner. We begin from x'_i at $i = 1$ and begin looping through i until $x'_{i'_L} = x'_i$, or $x'_{i'_R} = x'_i$. In the former case, we append the values of y'_i to $y_{i,\text{top}}(x'_i)$, and in the later case we append y'_i to $y_{i,\text{bot}}(x'_i)$. This process iterates until we reach $i = N_p$.

Next, we use the 'scipy.interpolate' subpackage (Virtanen *et al.* 2020) to interpolate between $y'_{i,\text{top}}(x'_i)$ and $y'_{i,\text{bot}}(x'_i)$ using an array of points linearly spaced between $x'_{i'_L}$ and $x'_{i'_R}$, thus creating two new arrays $y''_{\text{top}}(x'_i)$ and $y''_{\text{bot}}(x'_i)$ of the y' coordinates corresponding to $\{x'_i\}$. This allows us to create vertical slices (along the y' -axis), and then we average over the sum of the slices to obtain our width,

$$w = \frac{1}{N_x} \sum_{i=1}^{N_p} \left| y''_{\text{top}}(x'_i) - y''_{\text{bot}}(x'_i) \right|, \quad (\text{B1})$$

where $N_x = 50$ is the number of points we use to generate the interpolator. We have found this method to yield a more robust estimate of w in comparison with just using a slice (e.g., $w \approx |y''_{\text{top}}(x'_s) - y''_{\text{bot}}(x'_s)|$ at location $x'_s = \frac{1}{2}|x'_{i'_L} - x'_{i'_R}|$) or averaging using the number of available pixels only. The reason for that is that the width of the sheet can vary along the length.

Appendix C. Algorithm for calculating the parameters of a circle fitted through three points

Here, we summarize the algorithm that we use to calculate the radius of curvature of a given current sheet and the centre of the circle. The algorithm is based on

the curve fitting algorithms listed in Umbach & Jones (2003). More sophisticated methods, using more than three points, could also be used to obtain a ‘best fit’ circle instead.

We begin by choosing three points in our current sheet; the first two are x'_{i_L} and x'_{i_R} described above, and the third point is obtained by first calculating the half width at the centre of the sheet using (B1); i.e., $y_h = 1/2|y''_{top}(x'_s) - y''_{bot}(x'_s)|$ at location $x'_s = \frac{1}{2}|x'_{i_L} - x'_{i_R}|$. Then we obtain the midpoint $y_m = y_h + y''_{bot}(x'_s)$. These points are marked by red dots in figure 3. Next we map the three points into the complex numbers (z'_1, z'_2, z'_3) ; using the definition $z' = x' + \sqrt{-1}y'$.

We then apply a linear transformation to (z'_1, z'_2, z'_3) ; i.e.,

$$z'_j \rightarrow \frac{z'_j - z'_1}{z'_2 - z'_1}, \quad (\text{C1})$$

which results in $z'_1 \rightarrow 0$, $z'_2 \rightarrow 1$ and $z'_3 \rightarrow (z'_3 - z'_1)/(z'_2 - z'_1) \equiv u$. Here z'_1 is the left-hand point of the structure, z'_2 is the right-hand point of the structure and finally, z'_3 is the middle point in the structure.

We can then use the relationship $|z'_j - C| = r_c$ (where r_c is the radius of curvature of the circle fit, C is the coordinates of the circle’s centre, and $j \in \{1, 2, 3\}$) to obtain the following system of equations:

$$|z'_1 - C|^2 = |C|^2 = r_c^2 \quad (\text{C2})$$

$$|z'_2 - C|^2 = 1 - C - \bar{C} + |C|^2 = r_c^2 \quad (\text{C3})$$

$$|z'_3 - C|^2 = |u|^2 - \bar{u}C - u\bar{C} + |C|^2 = r_c^2. \quad (\text{C4})$$

We solve C from (C2)–(C4). The centre of the circle is then

$$C = \frac{u - |u|^2}{u - \bar{u}}. \quad (\text{C5})$$

Finally, we undo the linear transformation, which yields the centre of the circle in our original coordinates,

$$C \rightarrow (z'_2 - z'_1) \frac{u - |u|^2}{u - \bar{u}} + z'_1. \quad (\text{C6})$$

Therefore, we now have C , and using (C2), we obtain the radius of curvature, r_c .

REFERENCES

- ATOYAN, A.M. 1999 Radio spectrum of the crab nebula as an evidence for fast initial spin of its pulsar. *A&A* **346**, L49–L52, arXiv: [astro-ph/9905204](https://arxiv.org/abs/astro-ph/9905204).
- AZIZABADI, A.C., JAIN, N. & BÜCHNER, J. 2021 Identification and characterization of current sheets in collisionless plasma turbulence. *Phys. Plasmas* **28** (5), 052904.
- BALL, D., SIRONI, L. & ÖZEL, F. 2018 Electron and proton acceleration in trans-relativistic magnetic reconnection: dependence on plasma beta and magnetization. *Astrophys. J.* **862** (1), 80. arXiv: [1803.05556](https://arxiv.org/abs/1803.05556).

- BERESNYAK, A. 2019 Mhd turbulence. *Living Rev. Comput. Astrophys.* **5** (1), 2.
- BISKAMP, D. 2008 Magnetohydrodynamic turbulence. Cambridge, UK, Cambridge University Press, 1–297.
- BORGOGNO, D., GRASSO, D., ACHILLI, B., ROMÉ, M. & COMISSO, L. 2022 Coexistence of plasmoid and Kelvin–Helmholtz instabilities in collisionless plasma turbulence. *Astrophys. J.* **929** (1), 62.
- BUSOV, M. & NÄTTILÄ, J. 2021 Segmentation of turbulent computational fluid dynamics simulations with unsupervised ensemble learning. *Signal Process. Image Commun.* **99**, 116450. arXiv: [2109.01381](https://arxiv.org/abs/2109.01381).
- CHERNOGLAZOV, A., HAKOBYAN, H. & PHILIPPOV, A. 2023 High-energy radiation and ion acceleration in three-dimensional relativistic magnetic reconnection with strong synchrotron cooling. *Astrophys. J.* **959** (2), 122.
- CHERNOGLAZOV, A., RIPPERDA, B. & PHILIPPOV, A. 2021 Dynamic alignment and plasmoid formation in relativistic magnetohydrodynamic turbulence. *Astrophys. J. Lett.* **923** (1), L13.
- COMISSO, L. & JIANG, B. 2023 Pitch-angle anisotropy imprinted by relativistic magnetic reconnection. *Astrophys. J.* **959** (2), 137.
- COMISSO, L. & SIRONI, L. 2018 Particle acceleration in relativistic plasma turbulence. *Phys. Rev. Lett.* **121** (25), 255101. arXiv: [1809.01168](https://arxiv.org/abs/1809.01168).
- COMISSO, L. & SIRONI, L. 2019 The interplay of magnetically dominated turbulence and magnetic reconnection in producing nonthermal particles. *Astrophys. J.* **886** (2), 122. arXiv: [1909](https://arxiv.org/abs/1909).
- DAVIS, Z., COMISSO, L. & GIANNIOS, D. 2024 Intermittency and dissipative structures arising from relativistic magnetized turbulence. *Astrophys. J.* **964** (1), 14.
- Event Horizon Telescope Collaboration et al. 2019 *First M87 event horizon telescope results. V. Physical origin of the asymmetric ring*. *ApJ* **875** (1), L5.
- GALISHNIKOVA, A., PHILIPPOV, A., QUATAERT, E., BACCHINI, F., PARFREY, K. & RIPPERDA, B. 2023 Collisionless accretion onto black holes: dynamics and flares. *Phys. Rev. Lett.* **130** (11), 115201. arXiv: [2212.02583](https://arxiv.org/abs/2212.02583).
- GILLIES, S., VAN DER WEL, C., VAN DEN BOSSCHE, J., TAVES, M.W., ARNOTT, J., WARD, B.C. & Others 2024 Shapely. 2.0.0. Zenodo. DOI: [10.5281/zenodo.7428463](https://doi.org/10.5281/zenodo.7428463).
- GOLDREICH, P. & SRIDHAR, S. 1995 Toward a theory of interstellar turbulence. II. strong alfvénic turbulence. *Astrophys. J.* **438**, 763.
- HA, T., NÄTTILÄ, J., DAELAAR, J. & SIRONI, L. 2024 Machine-learning characterization of intermittency in plasma turbulence: single and double sheet structures. arXiv e-prints. arXiv: [2410.01878](https://arxiv.org/abs/2410.01878).
- HOWES, G.G. 2010 A prescription for the turbulent heating of astrophysical plasmas. *Mon. Not. R. Astron. Soc.: Lett.* **409** (1), L104–L108, arXiv: [1009.4212](https://arxiv.org/abs/1009.4212).
- HOWES, G.G. 2016 The dynamical generation of current sheets in astrophysical plasma turbulence. *Astrophys. J. Lett.* **827** (2), L28.
- IMBROGNO, M., MERINGOLO, C., SERVIDIO, S., CRUZ-OSORIO, A., CERUTTI, B. & PEGORARO, F. 2024 Long-lived equilibria in kinetic astrophysical plasma turbulence. *Astrophys. J. Lett.* **972** (1), L5.
- KAWAZURA, Y., BARNES, M. & SCHEKOCHIHIN, A.A. 2019 Thermal disequilibrium of ions and electrons by collisionless plasma turbulence. *Proc. Natl Acad. Sci.* **116** (3), 771–776. arXiv: [1807.07702](https://arxiv.org/abs/1807.07702).
- KEMPSKI, P., FIELDING, D.B., QUATAERT, E., GALISHNIKOVA, A.K., KUNZ, M.W., PHILIPPOV, A.A. & RIPPERDA, B. 2023 Cosmic ray transport in large-amplitude turbulence with small-scale field reversals. *Mon. Not. R. Astron. Soc.* **525** (4), 4985–4998. arXiv: [2304.12335](https://arxiv.org/abs/2304.12335).
- KENNEL, C.F. & CORONITI, F.V. 1984a confinement of the crab pulsar’s wind by its supernova remnant. *Astrophys. J.* **283**, 694–709.
- KENNEL, C.F. & CORONITI, F.V. 1984b magnetohydrodynamic model of crab nebula radiation. *Astrophys. J.* **283**, 710–730.
- KOHONEN, T. 2001 *Self-Organizing Maps*. Springer Berlin Heidelberg.
- KOHONEN, T. 2013 Essentials of the self-organizing map. *Neural Networks* **37**, 52–65.
- LEMOINE, M. 2023 Particle transport through localized interactions with sharp magnetic field bends in MHD turbulence. *J. Plasma Phys.* **89** (5), 2304–03023.

- LOUREIRO, N.F. & BOLDYREV, S. 2017 Collisionless reconnection in magnetohydrodynamic and kinetic turbulence. *Astrophys. J.* **850** (2), 182.
- LUO, Y., LYUTIKOV, M., TEMIM, T. & COMISSO, L. 2020 Turbulent model of crab nebula radiation. *Astrophys. J.* **896** (2), 147. arXiv: [2005.06319](https://arxiv.org/abs/2005.06319).
- MAKWANA, K.D., ZHDANKIN, V., LI, H., DAUGHTON, W. & CATTANEO, F. 2015 Energy dynamics and current sheet structure in fluid and kinetic simulations of decaying magnetohydrodynamic turbulence. *Phys. Plasmas* **22** (4), 042902.
- MALLET, A., SCHEKOCHIHIN, A.A. & CHANDRAN, B.D.G. 2017 Disruption of alfvénic turbulence by magnetic reconnection in a collisionless plasma. *J. Plasma Phys.* **83** (6), 905830609.
- MERINGOLO, C., CRUZ-OSORIO, A., REZZOLLA, L. & SERVIDIO, S. 2023 Microphysical plasma relations from special-relativistic turbulence. *Astrophys. J.* **944** (2), 122.
- MOŚCIBRODZKA, M., FALCKE, H. & SHIOKAWA, H. 2016 General relativistic magnetohydrodynamical simulations of the jet in M. *Astron. Astrophys.* **586**, A38. arXiv: [1510.07243](https://arxiv.org/abs/1510.07243).
- NÄTTILÄ, J. 2022 Runko: modern multiphysics toolbox for plasma simulations. *Astron. Astrophys.* **664**, A68.
- NÄTTILÄ, J. 2024 Radiative plasma simulations of black hole accretion flow coronae in the hard and soft states. *Nat. Commun.* **15** (1), 7026.
- NÄTTILÄ, J. & BELOBORODOV, A.M. 2021 Radiative turbulent flares in magnetically dominated plasmas. *Astrophys. J.* **921** (1), 87. arXiv: [2012.03043](https://arxiv.org/abs/2012.03043).
- NÄTTILÄ, J. & BELOBORODOV, A.M. 2022 Heating of magnetically dominated plasma by alfvén-wave turbulence. *Phys. Rev. Lett.* **128** (7), 075101.
- NURISSE, M., CELOTTI, A., MIGNONE, A. & BODO, G. 2023 Particle acceleration with magnetic reconnection in large-scale RMHD simulations—I. current sheet identification and characterization. *Mon. Not. R. Astron. Soc.* **522** (4), 5517–5528.
- PARASHAR, T.N. & MATTHAEUS, W.H. 2016 Propinquity of current and vortex structures: effects on collisionless plasma heating. *Astrophys. J.* **832** (1), 57.
- REES, M.J. & GUNN, J.E. 1974 The origin of the magnetic field and relativistic particles in the crab nebula. *Mon. Not. R. Astron. Soc.* **167** (1), 1–12.
- RIPPERDA, B., MAHLMANN, J.F., CHERNOGLAZOV, A., TENBARGE, J.M., MOST, E.R., JUNO, J., YUAN, Y., PHILIPPOV, A.A. & BHATTACHARJEE, A. 2021 Weak alfvénic turbulence in relativistic plasmas. Part 2. current sheets and dissipation. *J. Plasma Phys.* **87** (5), 905870512. arXiv: [2105.01145](https://arxiv.org/abs/2105.01145).
- ROSS, J. & LATTER, H.N. 2018 Dissipative structures in magnetorotational turbulence. *Mon. Not. R. Astron. Soc.* **477** (3), 3329–3342.
- RUSZKOWSKI, M. & PFROMMER, C. 2023 Cosmic ray feedback in galaxies and galaxy clusters. *Astron. Astrophys. Rev.* **31** (1), 4.
- SCHEKOCHIHIN, A.A. 2022 MHD turbulence: a biased review. *J. Plasma Phys.* **88** (5), 155880501.
- SERVIDIO, S., MATTHAEUS, W.H., SHAY, M.A., DMITRUK, P., CASSAK, P.A. & WAN, M. 2010 Statistics of magnetic reconnection in two-dimensional magnetohydrodynamic turbulence. *Phys. Plasmas* **17** (3), 032315.
- SINGH, D., FRENCH, O., GUO, F. & LI, X. 2024 Low-energy injection and nonthermal particle acceleration in relativistic magnetic turbulence. *Astrophys. J.* **979** (1), 39.
- SISTI, M., FADANELLI, S., CERRI, S.S., FAGANELLO, M., CALIFANO, F. & AGULLO, O. 2021 Characterizing current structures in 3D hybrid-kinetic simulations of plasma turbulence. *Astron. Astrophys.* **655**, A107.
- TENBARGE, J.M. & HOWES, G.G. 2013 Current sheets and collisionless damping in kinetic plasma turbulence. *Astrophys. J. Lett.* **771** (2), L27.
- UMBACH, D. & JONES, K.N. 2003 A few methods for fitting circles to data. *IEEE Trans. Instrum. Meas.* **52** (6), 1881–1885.
- URITSKY, V.M., POUQUET, A., ROSENBERG, D., MININNI, P.D. & DONOVAN, E.F. 2010 Structures in magnetohydrodynamic turbulence: detection and scaling. *Phys. Rev. E* **82** (5), 056326.
- VEGA, C., BOLDYREV, S., ROYTERSHEYN, V. & MEDVEDEV, M. 2022 Turbulence and particle acceleration in a relativistic plasma. *Astrophys. J. Lett.* **924** (1), L19.

- VIRTANEN, P. *et al.* 2020 Paul & SciPy 1.0 Contributors 2020 SciPy 1.0: fundamental algorithms for scientific computing in python. *Nat. Methods* **17** (3), 261–272.
- VLAHOS, L. & ISLIKER, H. 2023 Formation and evolution of coherent structures in 3D strongly turbulent magnetized plasmas. *Phys. Plasmas* **30** (4), 040502.
- WAN, M., MATTHAEUS, W.H., KARIMABADI, H., ROYTERSHEYN, V., SHAY, M., WU, P., DAUGHTON, W., LORING, B. & CHAPMAN, S.C. 2012 Intermittent dissipation at kinetic scales in collisionless plasma turbulence. *Phys. Rev. Lett.* **109** (19), 195001.
- WERNER, G.R., UZDENSKY, D.A., BEGELMAN, M.C., CERUTTI, B. & NALEWAJKO, K. 2018 Non-thermal particle acceleration in collisionless relativistic electron-proton reconnection. *Mon. Not. R. Astron. Soc.* **473** (4), 4840–4861. arXiv: [1612.04493](https://arxiv.org/abs/1612.04493).
- ZHDANKIN, V., BOLDYREV, S., PEREZ, J.C. & TOBIAS, S.M. 2014 Energy dissipation in magnetohydrodynamic turbulence: coherent structures or “nanoflares”? *Astrophys. J.* **795** (2), 127.
- ZHDANKIN, V., BOLDYREV, S. & UZDENSKY, D.A. 2016 Scalings of intermittent structures in magnetohydrodynamic turbulence. *Phys. Plasmas* **23** (5), 055705. arXiv: [1602.05289](https://arxiv.org/abs/1602.05289).
- ZHDANKIN, V., UZDENSKY, D.A., PEREZ, J.C. & BOLDYREV, S. 2013 Statistical analysis of current sheets in three-dimensional magnetohydrodynamic turbulence. *Astrophys. J.* **771** (2), 124. arXiv: [1302.1460](https://arxiv.org/abs/1302.1460).
- ZHDANKIN, V., WALKER, J., BOLDYREV, S. & LESUR, G. 2017*a* Universal small-scale structure in turbulence driven by magnetorotational instability. *Mon. Not. R. Astron. Soc.* **467** (3), 3620–3627. arXiv: [1702.02857](https://arxiv.org/abs/1702.02857).
- ZHDANKIN, V., WERNER, G.R., UZDENSKY, D.A. & BEGELMAN, M.C. 2017*b* Kinetic turbulence in relativistic plasma: from thermal bath to nonthermal continuum. *Phys. Rev. Lett.* **118** (5), 055103. arXiv: [1609.04851](https://arxiv.org/abs/1609.04851).